





## Atmospheric concentrations of black carbon are substantially higher in spring than summer in the Arctic

Zsófia Jurányi <sup>1✉</sup>, Marco Zanatta<sup>1,5</sup>, Marianne T. Lund <sup>2</sup>, Bjørn H. Samset <sup>2</sup>, Ragnhild B. Skeie <sup>2</sup>, Sangeeta Sharma<sup>3</sup>, Manfred Wendisch<sup>4</sup> & Andreas Herber<sup>1</sup>

A key driving factor behind rapid Arctic climate change is black carbon, the atmospheric aerosol that most efficiently absorbs sunlight. Our knowledge about black carbon in the Arctic is scarce, mainly limited to long-term measurements of a few ground stations and snap-shots by aircraft observations. Here, we combine observations from aircraft campaigns performed over nine years, and present vertically resolved average black carbon properties. A factor of four higher black carbon mass concentration (21.6 ng m<sup>-3</sup> average, 14.3 ng m<sup>-3</sup> median) was found in spring, compared to summer (4.7 ng m<sup>-3</sup> average, 3.9 ng m<sup>-3</sup> median). In spring, much higher inter-annual and geographic variability prevailed compared to the stable situation in summer. The shape of the black carbon size distributions remained constant between seasons with an average mass mean diameter of 202 nm in spring and 210 nm in summer. Comparison between observations and concentrations simulated by a global model shows notable discrepancies, highlighting the need for further model developments and intensified measurements.

<sup>1</sup>Alfred Wegener Institute Helmholtz Centre for Polar and Marine Research, Bremerhaven, Germany. <sup>2</sup>CICERO Center for International Climate Research, Oslo, Norway. <sup>3</sup>Environment and Climate Change Canada, Science and Technology Branch, Climate Research Division, Toronto, ON, Canada. <sup>4</sup>Leipzig Institute for Meteorology, University of Leipzig, Leipzig, Germany. <sup>5</sup>Present address: Institute of Meteorology and Climate Research, Karlsruhe Institute of Technology, Karlsruhe, Germany. ✉email: [zsafia.juranyi@awi.de](mailto:zsafia.juranyi@awi.de)

During the past decades, the Arctic has experienced drastic climate changes, with a warming of more than twice the rate of the global average, the extent of sea-ice continuously decreasing, and permafrost regions thawing<sup>1,2</sup>. Apart from the warming caused by long-lived greenhouse gases, short-lived climate forcers such as black carbon (BC) aerosol particles may have a substantially contribution<sup>2,3</sup>. BC is an important constituent of the atmospheric aerosol, emitted by incomplete combustion processes of biomass or fossil fuels. BC is the most efficient aerosol component at absorbing visible light<sup>4</sup>, thereby playing an important role in the Earth's radiative energy balance. Suspended in the atmosphere, BC particles affect the Earth's climate system directly by absorbing and scattering solar radiation, indirectly by modifying microphysical and optical properties of clouds, and also through rapid adjustments initiated by local heating of the atmospheric column<sup>5</sup>. In addition, upon deposition on white surfaces such as snow and ice, BC particles can also significantly affect the local surface albedo.

In the Arctic, most aerosol particles and trace gases are characterized by a distinct seasonal variability with high concentrations in late winter and spring. This phenomenon is often referred to as "Arctic haze", a term firstly introduced by Mitchell<sup>6</sup>. It is caused by a combination of more efficient poleward transport of mid-latitude pollution and limited removal processes. The Arctic haze then disappears because of the increased removal by low-level clouds in summer<sup>7–10</sup>. Following the same seasonality, BC particle concentrations in the Arctic, measured at ground-based stations, also show the highest concentrations in late winter and spring and lowest in summer<sup>11–15</sup>. However, it was also shown that not all Arctic stations follow this cycle, Summit station in Greenland reports higher BC particle concentration in summer<sup>15</sup>.

Modeling studies show that most of the BC in the Arctic atmosphere originates from non-Arctic remote sources with contributions from the European and Asian emissions dominating near-surface concentrations, while those from East Asian emissions contribute mostly to the upper troposphere<sup>16–21</sup>. Freshly emitted BC particles are non-hygroscopic. During ageing, the BC particles increase in size and become increasingly hygroscopic<sup>22,23</sup>. With increasing hygroscopicity the chances of removal from the atmosphere via precipitation become higher, and therefore, most of the aged BC are scavenged before reaching the Arctic. However, those BC particles actually arriving in the Arctic may exert significant direct radiation and surface albedo effects, as these absorbing particles are found over highly reflecting snow/ice surfaces<sup>4,24,25</sup>.

Most observations of BC in the Arctic atmosphere originate from ground-based measurements collected at continuous monitoring sites. Only a few Arctic sites have long-term BC data-sets available, mainly in the form of aerosol absorption coefficient measurements<sup>26</sup>. In the last decade, measurements of the vertical distribution of BC properties have appeared as well. Aircraft measurements characterize BC properties at higher altitudes, although these capture only a snap-shot in time.

For example, airborne BC measurements were performed during the ARCPAC (Aerosol, Radiation, and Cloud Processes affecting Arctic Climate) campaign, based in Fairbanks, Alaska, in April 2008<sup>27,28</sup>. Furthermore, the HIAPER (High-performance Instrumented Airborne Platform for Environmental Research) Pole-to-Pole Observations (HIPPO,<sup>29</sup>) program performed aircraft transects along the Pacific from 85°N to 67°S measuring vertical profiles of BC properties. During the Airborne Extensive Regional Observations in Siberia (YAK-AEROSIB), BC measurements were collected over eastern and western Siberia<sup>30</sup>. The Atmospheric Tomography Mission performed global-scale,

in situ measurements including BC properties similarly to HIPPO between 2016 and 2018 collecting data over all four seasons<sup>31</sup>.

Starting in 2009, the Alfred Wegener Institute, Helmholtz Center for Polar and Marine Research organized almost annual aircraft campaigns in the Arctic to measure vertical profiles of BC properties. During the Polar Airborne Measurements and Arctic Regional Climate Model Simulation Project (PAMARCMiP) a series of aircraft campaigns focusing on BC measurements were conducted across the western Arctic<sup>32</sup>. The Network on Climate and Aerosols: Addressing Key Uncertainties in Remote Canadian Environments (NETCARE) covered two aircraft campaigns in the Canadian Arctic<sup>33</sup>, and as part of Arctic Amplification (AC)<sup>3</sup> Transregional Collaborative Research Centre<sup>34,35</sup> project, more airborne campaigns took place to characterize vertical profiles of BC in the Arctic.

Unmanned aerial vehicle and tethered balloon measurements can also provide us vertical BC profiles with excellent altitude resolutions and substantially lower expenses. However, these platforms cannot reach as high altitudes as aircraft, can only have smaller payload and such measurements can only be performed at restricted locations. Tethered balloons were used to gain BC absorption coefficient profiles in Svalbard in Ny-Ålesund<sup>36,37</sup> and in Longyearbyen<sup>38</sup>. The unmanned aerial vehicle MANTA measured atmospheric aerosol properties including BC absorption coefficient up to 3000 m altitude from Ny-Ålesund<sup>39</sup>.

In addition to observations, there have been extensive modeling efforts to investigate Arctic aerosols, including BC, and their climate effects<sup>18,40,41</sup>. Simulations can help supplementing the limited coverage of BC observations, especially at higher altitudes. Previous studies have shown that numerous models struggle to reproduce the characteristics of observed seasonal variations. In particular, they often underestimate the concentration of BC during spring<sup>42–45</sup>. As a consequence, further research efforts are required to improve BC concentration estimates by updating emission inventories and improving parameter settings in the models.

In this study, we present results from a series of aircraft BC measurements performed between 2009 and 2017 by single particle soot photometers (SP2). These campaigns provide the largest available Arctic BC aircraft data set to date presented as a whole, covering the European and Canadian Arctic. The main aim is to compile a representative reference data set of Arctic BC properties at different altitudes. The analysis presented here is focused on the seasonal differences between spring and summer. We also explore the representativeness of this data set for the entire European and Canadian Arctic. This comprehensive data set offers unique possibilities for the modeling community to validate, verify, and adapt their products. Additionally, we show as an example a comparison between the observations and the output of the OsloCTM3 chemical transport model.

## Results and discussion

An innovative method was developed and applied to average, sort and classify our large data set of airborne BC measurements. This included dividing the measurement area into so-called four-dimensional grid cells, and collecting all performed BC measurements within these grids, irrespective of the flight pattern. This resulted in an average of about 20 min of BC measurements per grid. Each four-dimensional grid is defined as 5° latitude times 5° longitude times 500 m altitude times 1-year unit (see Methods section for more details on the data treatment). Grids containing at least 400 BC particles were kept and averaged, grids with less data were discarded. This resulted in all together 422 grid cells with data in spring and 85 in summer.

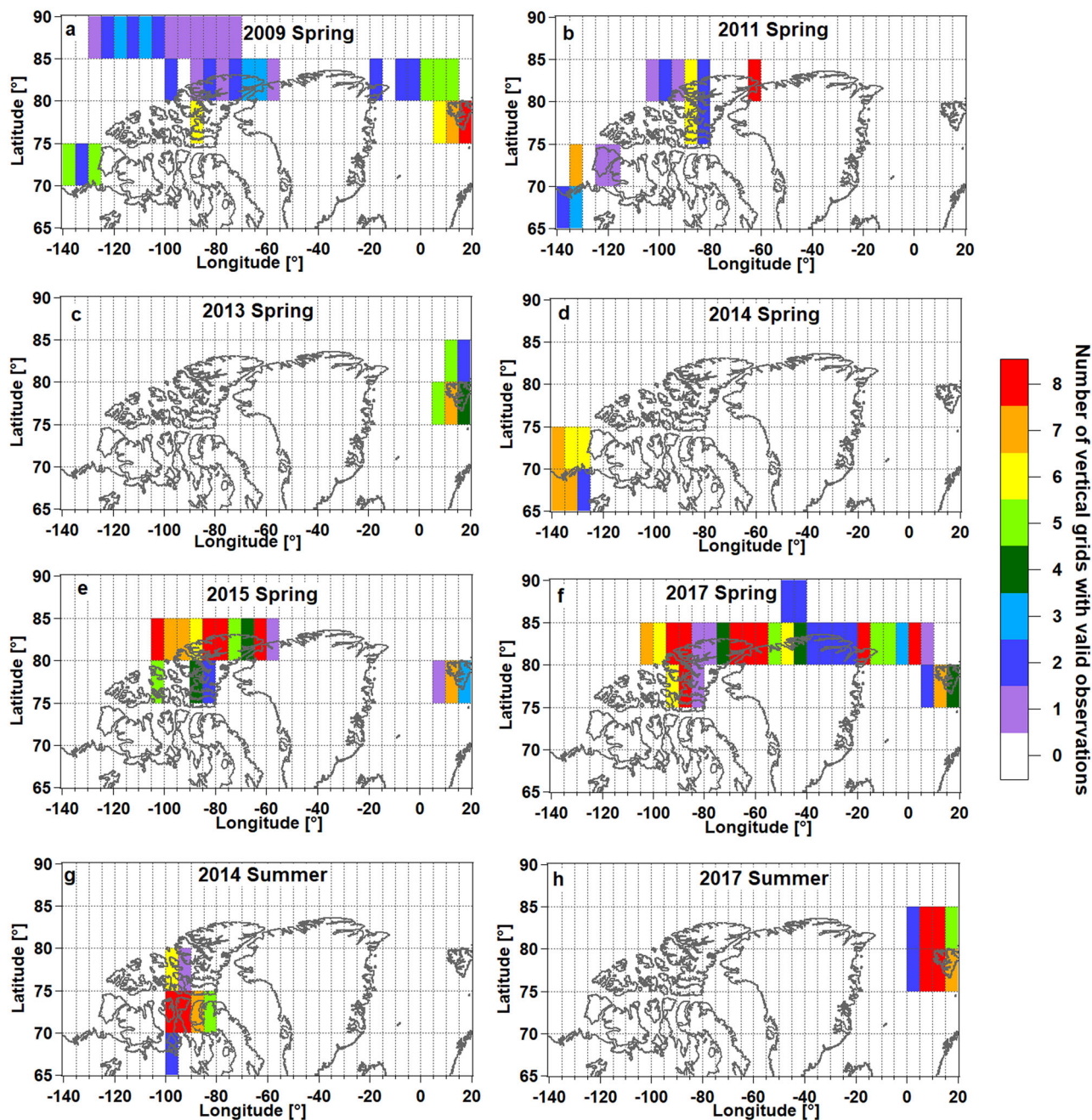


**Fig. 1** BC data availability at different locations during the various aircraft campaigns. The (a–f) show spring data, (g and h) summer data. Colored areas: valid data is available; the different colors indicate the number of altitude grids with data. White areas: no or not enough BC data could be collected.

Figure 1 shows the data availability in the grid cells for the different measurement campaigns. The number of grids, where sufficient amount of data was acquired, are presented in color coding. A white background indicates lack of, or not sufficient data at any altitude bin in the vertical column. Note that the aircraft campaigns in the different years within a season can have a different temporal coverage (see Table 1 for the exact campaign durations). Some of the flight campaigns, such as the spring campaign in 2009 (Fig. 1a) cover a broad geographical area, whereas in some years the flights were much more localized (e.g., 2013 Spring, Fig. 1c).

**Seasonality of BC properties.** In the following we focus on the differences and similarities between the summer and spring BC properties. For this purpose, in each grid cell including all

locations, altitudes and campaign years, the respective BC properties were derived, and their statistical characteristics over all grids were calculated. Figure 2 shows a boxplot with average, median, and percentile values of BC properties. To be comparable with past and future BC studies, we report a greater selection of different BC properties, these are partially not independent from each other, and therefore, not each of them are discussed in the following. The BC mass equivalent diameters were calculated from particle mass assuming a void-free spherical shape and a density of  $1800 \text{ kg m}^{-3}$ . These are the mass mean diameter ( $D_{m_{BC}}$ ), median diameter of the BC mass size distribution ( $D_{50m_{BC}}$ ), the number mean diameter ( $D_{n_{BC}}$ ), and median diameter of the BC number size distribution ( $D_{50n_{BC}}$ ). In addition, the interquartile ranges of the number (IQR<sub>n</sub>) and mass size distributions (IQR<sub>m</sub>), and the geometrical standard deviations of



**Table 1** List of the performed aircraft campaigns with duration, aircraft operation base and reference to the data-base of the corresponding aircraft tracks.

Campaign	Duration	Season	Operation base	SP2 Data	Reference
PAMARCMiP 2009	04.04-04.16	Spring	Longyearbyen, Alert, Eureka, Resolute Bay	1654 min	32,80
PAMARCMiP 2011	03.31-04.22	Spring	Longyearbyen, Station Nord, Alert, Eureka, Inuvik	809 min	32
PAMARCMiP 2013	04.18-04.21	Spring	Longyearbyen	311 min	32
RACEPAC 2014	05.01-05.23	Spring	Inuvik	1564 min	-
NETCARE 2014	07.03-07.20	Summer	Resolute Bay	1490 min	33
NETCARE 2015	04.05-04.13	Spring	Longyearbyen, Alert, Eureka	1474 min	33
PAMARCMiP 2017	03.20-04.13	Spring	Longyearbyen, Alert, Eureka	1876 min	32
ACLOUD 2017	05.27-06.26	Summer	Longyearbyen	2068 min	34,71

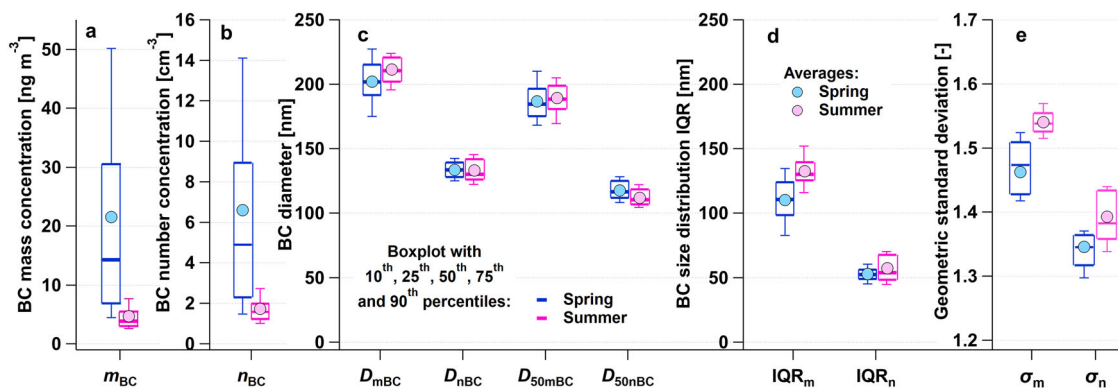


**Fig. 2** Boxplot of BC properties in the different grids. The boxplot represents data from spring (blue) and from summer (pink) showing 10th, 25th, 50th, 75th and 90th percentiles. The round blue and pink markers show the averages. **a** Shows the statistics of the BC mass concentration ( $m_{BC}$ ), **(b)** the BC number concentration ( $n_{BC}$ ), **(c)** the different BC diameters ( $D_{mBC}$ ,  $D_{nBC}$ ,  $D_{50mBC}$ ,  $D_{50nBC}$ ), **(d)** the size distribution interquartile ranges ( $IQR_m$ ,  $IQR_n$ ) and **(e)** the size distribution geometric standard deviations ( $\sigma_m$ ,  $\sigma_n$ ).

**Table 2** List and description of the derived BC parameters.

Parameter	Abbreviation	Formula	Remark
BC mass of single particle	$M_{BC}$	-	Directly measured by the SP2
BC mass equivalent diameter	$D$	$(6M_{BC}/\pi\rho)^{1/3}$	Using void-free density of $\rho = 1.8 \text{ g cm}^{-3}$
BC mass concentration	$m_{BC}$	-	Total mass of all BC particles per volume unit of air
BC number concentration	$n_{BC}$	-	Total number of BC particles per volume unit of air
BC mass size distribution	msd	$dm_{BC}/d\log D$	-
BC number size distribution	nsd	$dn_{BC}/d\log D$	-
BC mass mean diameter	$D_{mBC}$	$\frac{\int_0^{D_{max}} D \cdot \text{msd}(D) \cdot d\log D}{\int_0^{D_{max}} \text{msd}(D) \cdot d\log D}$	Mean diameter of the mass size distribution
BC number mean diameter	$D_{nBC}$	$\frac{\int_0^{D_{max}} D \cdot \text{nsd}(D) \cdot d\log D}{\int_0^{D_{max}} \text{nsd}(D) \cdot d\log D}$	Mean diameter of the number size distribution
BC mass median diameter	$D_{50mBC}$	-	Median diameter of the BC mass size distribution
BC number median diameter	$D_{50nBC}$	-	Median diameter of the BC number size distribution
BC msd interquartile range	$IQR_m$	-	Difference of the 75th and 25th percentiles of msd
BC nsd interquartile range	$IQR_n$	-	Difference of the 75th and 25th percentiles of nsd
BC msd geometric standard deviation	$\sigma_m$	$\exp \left[ \left( \frac{\int_0^{D_{max}} \text{msd}(D) \cdot (\log D - \log D_{gm})^2 \cdot d\log D}{m_{BC}} \right)^{1/2} \right]$	Where $D_{gm}$ is the geometric mean diameter of msd
BC nsd geometric standard deviation	$\sigma_n$	$\exp \left[ \left( \frac{\int_0^{D_{max}} \text{nsd}(D) \cdot (\log D - \log D_{gn})^2 \cdot d\log D}{n_{BC}} \right)^{1/2} \right]$	Where $D_{gn}$ is the geometric mean diameter of nsd

the number ( $\sigma_n$ ) and mass size distributions ( $\sigma_m$ ) were calculated for each grid cell, serving as indicators for the width of the size distributions. The exact definition of the derived BC parameters can be found in Table 2. Their derived statistical measures are shown in Fig. 2 and in Supplementary Table S1.

The median  $m_{BC}$  in spring is  $14.3 \text{ ng m}^{-3}$  with the interquartile range of  $7.0 \text{ ng m}^{-3}$ – $30.6 \text{ ng m}^{-3}$ , whereas the summer value is almost a factor four lower with a median of  $3.9 \text{ ng m}^{-3}$  and an interquartile range of  $3.1 \text{ ng m}^{-3}$ – $5.5 \text{ ng m}^{-3}$  (Fig. 2a). Such seasonal variability, with much higher BC concentrations during

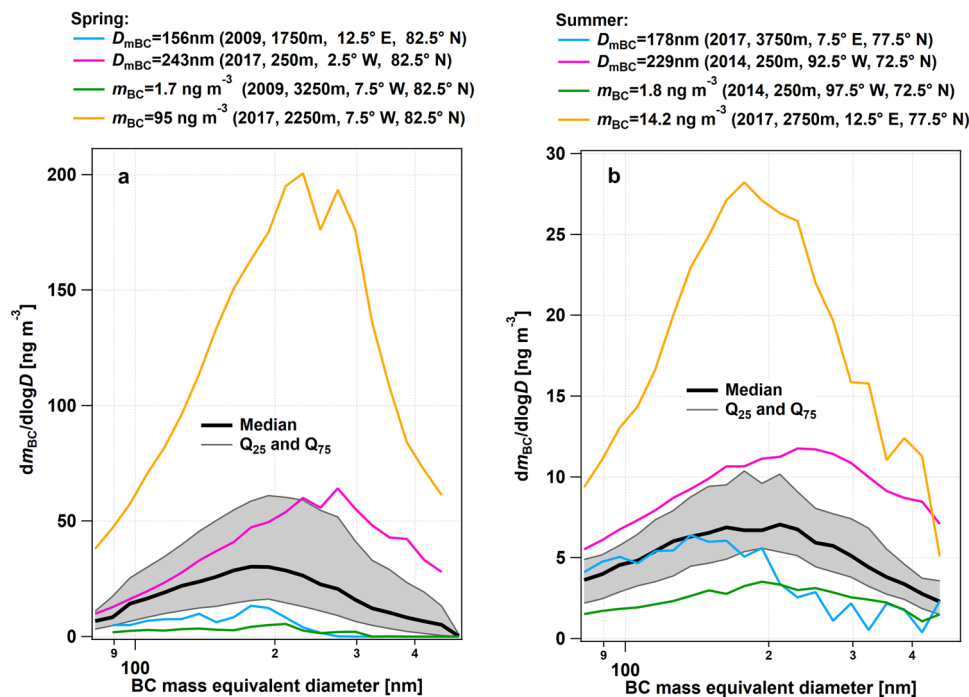


**Fig. 3 Measured BC mass size distributions.** **a** Shows spring and **(b)** summer data. The black line with gray shading shows the median, 25th and 75th percentiles over all grids, the colored lines show the mass size distributions in presence of extreme BC mass concentrations ( $m_{BC}$ ) and BC mass mean diameters ( $D_{mBC}$ ). The bracketed values in the label indicate the year of measurement, the central altitude, the central longitude and central latitude of the grid where the extreme BC property value was observed.

spring compared to summer, is expected and has been reported previously<sup>12–14</sup>. Next to the observed seasonal difference of the median  $m_{BC}$ , its wide interquartile range observed in spring indicates strong location-to-location, altitude, and year-to-year variability. In summer, the  $m_{BC}$  remains almost constant at the different locations, altitudes and years. However, the summer data originate from 2 years and cover a far smaller geographical area than the spring campaigns. The number concentration of BC-containing particles shows a behavior similar to  $m_{BC}$ ;  $n_{BC}$  is much higher in spring than in summer with median values of  $4.9 \text{ cm}^{-3}$  and  $1.6 \text{ cm}^{-3}$ , respectively (Fig. 2b).

We compare this seasonality to long-term, ground-based, stationary measurements of equivalent BC<sup>46</sup> that are based on absorption measurements by an Aethalometer. The equivalent BC mass concentrations measured at Alert and Utqiagvik (Barrow) in the Canadian Arctic between 1989 and 2002<sup>11,12</sup> revealed a seasonal variability with a factor of 10 difference between the highest (in spring) and lowest (in summer) values. A similar factor was found in the European Arctic at the Zeppelin station<sup>13</sup>. Furthermore, the seasonal variability of aerosol optical properties at six different Arctic stations was investigated<sup>15</sup>, from which three stations (Alert in Canada, Summit in Greenland and Zeppelin in Svalbard) are situated in the area where our measurements are located (from now on, this area will be called region of our interest, ROI, see exact definition in Methods) and one (Utqiagvik /Barrow in Alaska) just right outside of it. The seasonal variability of the absorption coefficient (with BC being responsible for most of it) showed highest values in spring and lowest in summer at most stations, similar to the measurements presented here.

There are a few existing, altitude-resolved BC studies based on SP2 measurements, comparing  $m_{BC}$  in summer and spring, and these also reported higher concentrations in spring. It was shown that  $31.5 \text{ ng m}^{-3}$  and  $30.1 \text{ ng m}^{-3}$  BC were present around Alert and Eureka stations in spring 2015, while  $<1.4 \text{ ng m}^{-3}$   $m_{BC}$  was

measured around Resolute Bay in summer 2014<sup>33</sup>. Please note that the aircraft data from this study are included in our current study as well. The SP2 BC measurements conducted during the HIPPO aircraft campaigns along the Pacific also revealed the highest concentrations at all altitudes in the spring season in the Arctic<sup>47</sup>.

Contrary to the pronounced seasonal difference in the BC mass and number concentrations, we cannot identify any notable seasonal difference neither in the average BC size (Fig. 2c) nor in the shape of the size distribution (black line in Fig. 3). The median of the mass mean diameter (202 nm in spring, 210 nm in summer) are similar in both seasons. The mass size distribution is on average broader in summer, the median of IQR<sub>m</sub> is 111 nm in spring and 130 nm in summer (Fig. 2d).

An increase in the BC mass concentration can be caused by the increase of BC particles' number and/or the increase of the BC particle size. In our data-set, the pronounced seasonal BC mass concentration difference appears to be solely a consequence of the increased number of BC particles reaching the region, not of changing BC particle size.

The size distribution of the BC particles only varies little between locations, altitude, years, and seasons, as indicated by the narrow distributions of the average BC size and size distribution width (Fig. 2c, d). The 25th percentile of the mass mean diameter is 192 nm in spring and 202 nm in summer, whereas the 75th percentile is 215 nm and 221 nm, respectively. Zanatta et al.<sup>48</sup> reported SP2 BC measurements with a mass size distribution around 240 nm peak size measured in spring 2012 at the ground-based station Zeppelin in Svalbard, whereas we have registered such high values only in a very few grid cells in spring, in particular at the lowest altitudes (0–500 m), around Svalbard, in the Fram Strait, or at the northwestern part of Greenland in 2017. On average, a modal mass diameter of 225 nm was measured<sup>49</sup> for BC during winter and 170 nm during summer at Alert station between 2011 and 2013. At the same station, between January and May 2018, a modal diameter of the BC mass size distribution of

210 nm was reported<sup>50</sup>. Mass median diameters of the BC mass size distribution of around 170 nm were measured during ship-based observations in September in the Arctic Ocean and Bering Sea<sup>51</sup>. We have observed similar mass median values in summer around Svalbard. SP2 aircraft BC measurements performed during the PAMARCMiP aircraft campaign in spring 2018 in the Fram Strait provided BC measurements with mass median diameters between 168 and 228 nm<sup>52</sup>. Our derived values are also within this range with an average ( $\pm$  standard deviation) spring mass median diameter of 187 nm ( $\pm$ 16 nm).

The average values (round markers in Fig. 2) of all investigated BC properties (except the mass and number concentrations in spring) are close to the corresponding median values, which indicates that their distribution is nearly symmetrical. The averages of  $m_{BC}$  and  $n_{BC}$  are higher than the median in spring, which is a consequence of the few, very high BC values that were mainly present in 2014. As shown by the box and whiskers of Fig. 2a, b, strong variability in the concentration of BC particles was observed in spring, indicating the occurrence of different conditions.

Not only the amount of BC ( $m_{BC}$ ,  $n_{BC}$ ), but also their size distribution greatly influences the solar radiative forcing of BC<sup>53</sup>. Therefore, in the following, the BC mass size distributions in the individual grid cells will be investigated. We focus on the cases of extremes, to present the full variability of mass size distributions that were encountered during the measurements. As a comparison to the median (with 25th and 75th percentiles) BC mass size distribution (black line and gray shading in Fig. 3), the mass size distributions in the grid cells that are associated with a highest and lowest  $m_{BC}$  or  $D_{m_{BC}}$ , are shown in Fig. 3 as colored lines. Please note that a grid cell contains already average BC properties, and therefore, even higher or lower short-term extreme BC values might be present in the Arctic when the data are based on a higher time resolution.

The BC mass size distributions that belong to the grid cells with highest measured BC mass are shown in Fig. 3 as orange lines. In spring, the highest observed  $m_{BC}$  was  $94.5 \text{ ng m}^{-3}$ , measured in 2017 at an altitude of 2000–2500 m at the North-Eastern part of Greenland. In summer, the highest  $m_{BC}$  value was present in 2017, at an altitude of 2500–3000 m north of Svalbard. The highest measured mass concentration value in spring is more than a factor of six higher than in summer ( $14.2 \text{ ng m}^{-3}$ ), the shape of the size distribution is shifted to larger particles in spring. The lowest mass concentrations in spring and in summer (Fig. 3, green lines) are close to each other with  $m_{BC}$  of  $<2 \text{ ng m}^{-3}$ , the corresponding mass size distributions have similar shapes. This similarity suggests that the background BC concentrations are in both seasons similar, the previously shown distinct seasonal difference is probably a result of increased transport from lower latitudes in spring. The mass size distributions with the largest diameters (Fig. 3, purple lines, 243 nm in spring and 229 nm in summer) were measured in both seasons at the lowest altitude, but at different regions. The presence of the lowest  $D_{m_{BC}}$  (156 nm in spring and 178 nm in summer) was associated with low BC mass concentrations (Fig. 3, blue lines).

**Average and spatial variability of vertical profiles.** The altitude dependence of the different BC properties is investigated using a selection of the acquired BC measurements, to obtain unbiased average altitude profile. Only complete or close to complete profiles from different locations and measurement years were used in this analysis. Therefore, the average BC properties are calculated from values observed in the same location and year, independent of the altitude. In practice, for a certain longitude,

latitude and year values, grids with valid data at a minimum of six (out of the possible eight) different altitudes were kept. These data can be identified by searching in Fig. 1 for the geographical locations with at least six altitude grids having available measurements (yellow, orange or red colored grids). All together 35 altitude-dependent curves meet this criterion in spring, and nine in summer covering different locations within the ROI.

Figure 4 shows the average (round markers) and median (triangles) of these BC mass concentration altitude-dependent curves for spring (a) and for summer (b), the error bars indicate the standard deviation. The solid line shows the linear vertical fit to the averages. The linear fit was applied to the data to help the identification of the presence or absence of a vertical trend. It should not be treated as a parameterization. The vertical variability of  $m_{BC}$  in both seasons show similar features, they remain almost constant with altitude. In spring we identify an average decrease as determined by the slope of the linear fit of  $-1.1 \text{ ng m}^{-3} \text{ km}^{-1}$ , which translates to a 4.7% decrease per km. The same values in summer are  $-0.17 \text{ ng m}^{-3} \text{ km}^{-1}$  and 3.7% decrease per km, respectively. Both decreases are not statistically significant, the fit uncertainties are larger than the absolute value of the slopes. As a comparison, in Fig. 4 the average (gray solid line) and standard deviation (gray dashed line) of  $m_{BC}$  is also shown, using not only the complete or almost complete profiles but the entire data-set. The similarity of the two average  $m_{BC}$  profiles show that the used selection of the data represents well the entire data-set.

The spatial variability of BC vertical trends was investigated as function of longitude. Figure 5 shows the slopes of the linear fit on each of  $m_{BC}$  vertical profiles as a function of the longitude, at which the measurement was taken. The symbols indicate the different measurement latitudes, whereas the colors show the measurement years. Extremely high BC mass concentration slopes up to  $25 \text{ ng m}^{-3} \text{ km}^{-1}$  were measured in spring 2014 (orange markers), in the western part of the Canadian Arctic at latitudes between 65 and 75°N (lowest latitudes in the ROI). These data were greatly influenced by high BC concentrations appearing at upper altitudes (most probably originating from long-range transport), which resulted in the measured large slope values (above  $10 \text{ ng m}^{-3} \text{ km}^{-1}$ ). Excluding the exceptional 2014 event, the  $m_{BC}$ -altitude curves have slopes between  $-12 \text{ ng m}^{-3} \text{ km}^{-1}$  and  $3 \text{ ng m}^{-3} \text{ km}^{-1}$ . However, only two out of 29 slope values show a slight increase with altitude. Next to this, no relationship between the slope and latitude nor longitude, neither measurement year could be identified. In summer (Fig. 5b), the slope values are distributed between  $-1 \text{ ng m}^{-3} \text{ km}^{-1}$  and  $1 \text{ ng m}^{-3} \text{ km}^{-1}$ . The two data clusters from 2014 in the Canadian Arctic and from 2017 European Arctic (region Svalbard) look similar.

The average altitude dependence of  $D_{m_{BC}}$  is shown in Fig. 6 during spring (a) and summer (b) using the same data as for the altitude dependence investigation of  $m_{BC}$ . Here, we show the same comparison, as for the altitude dependence of  $m_{BC}$  using the entire data-set as well (gray lines in Fig. 6). In spring, the diameter decreases with the altitude from 214 to 194 nm with a slope of  $-5.3 \pm 3.4 \text{ nm km}^{-1}$ , as determined by a linear fit (green line). The summer season shows a slightly different behavior, with very similar diameters on average almost not changing with the altitude (slope of  $-1.4 \pm 2.2 \text{ nm km}^{-1}$ ). Between the lowest flight level (60 m) and 4000 m altitude, the BC particles become on average 5 nm smaller. BC size is both dependent on emission type and atmospheric processing. Freshly emitted, traffic related BC particles are on average smaller than, e.g., biomass burning particles. In addition, atmospheric aging can lead to increasing size as well<sup>54</sup>. On the other hand, Moteki et al.<sup>55</sup> found indication that larger BC particles are removed from the

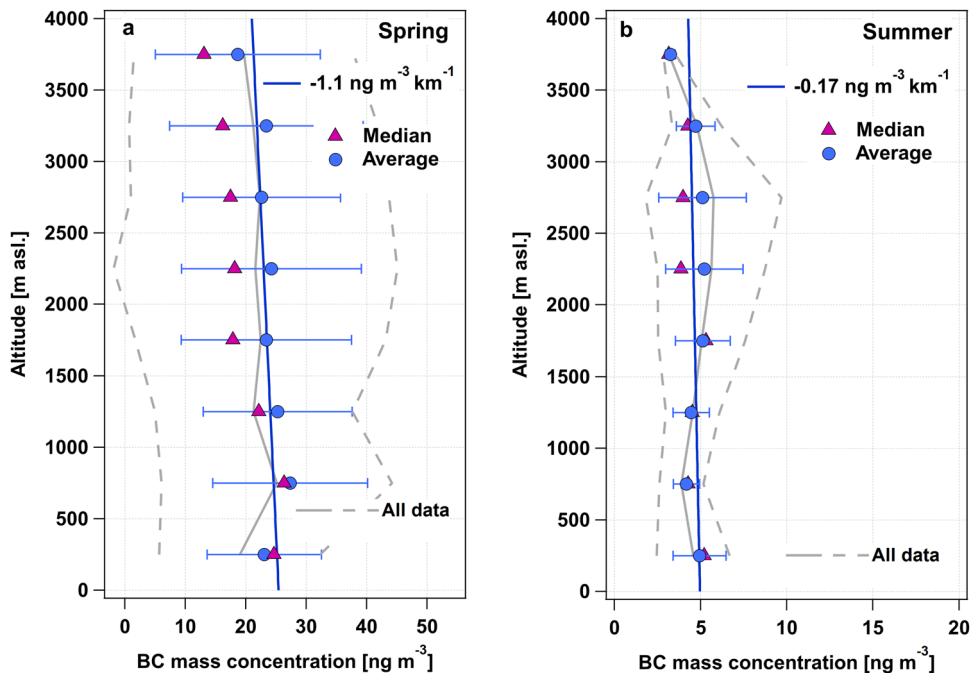


**Fig. 4** The altitude dependence of the BC mass concentration. Blue round markers show the average, purple triangles the median of the BC mass concentration in spring (a) and summer (b). The error bars indicate the standard deviation, the blue line shows the linear fit to the averages. The gray lines show the average (solid line) and standard deviation (dashed line) of the BC mass concentration altitude dependence, if the entire data-set is used including the incomplete profiles as well.

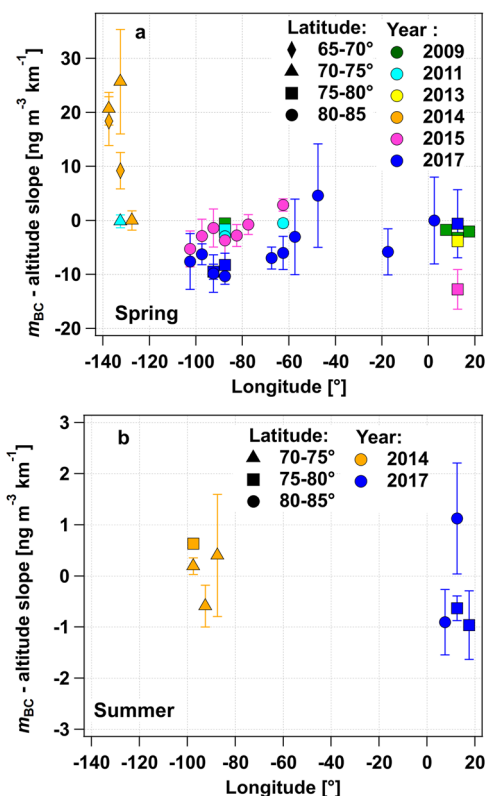


**Fig. 5** Slope of the location dependent BC mass concentration–altitude curves (determined by a linear fit) as function of the longitude. a Shows spring data, whereas (b) shows summer data. The colors indicate the measurement years, the markers the latitude regions. The error bars show the uncertainty of the determined fit slopes.

atmosphere with higher probability by wet deposition. Based solely on the altitude dependence of BC diameters we cannot decide which processes play an important role in the Arctic.

**Data representativeness.** A key question is how representative the sampled region is for a broader characterization of Arctic BC distribution. It is important to discuss if the data set, with many grids without having any data from (Fig. 1, grids with white color), is representative for the average BC properties of the European and Canadian Arctic. To investigate this issue, we follow two approaches: first, using only calculated  $m_{BC}$  from the OsloCTM3 model, and second, using the measured data set itself.

The first approach compares modeled BC profiles using only grid boxes where measurements exist (i.e., artificially flying through the model grids) versus using all grid boxes in the full ROI. Figure 7 shows the result of this comparison as function of the campaign year. A close agreement between the two approaches (flying through the model grid versus considering all grid cells) indicates that the restricted, grid-based data represent the entire ROI. However, it assumes that the model reproduces the spatial distribution of  $m_{BC}$  well. The modeled median  $m_{BC}$  agree well for most of the campaigns in both seasons; larger discrepancy could only be identified for the 2014 spring campaign. The data in question originate from the RACEPAC 2014 campaign (Table 1), which took place at the southernmost latitude, around Inuvik, Northwest Territories, Canada. The reason for the BC concentration differences was the unusually increased long-range transport from southern latitudes reaching the region of the measurement campaign. The altitude-dependent grid model predictions show high BC concentrations at all altitudes with the largest difference around 1000–1500 m comparing to the model values from the entire ROI. However, looking at the altitude-dependent measurements from 2014 spring, values close to the average spring BC concentrations are documented (considering all spring



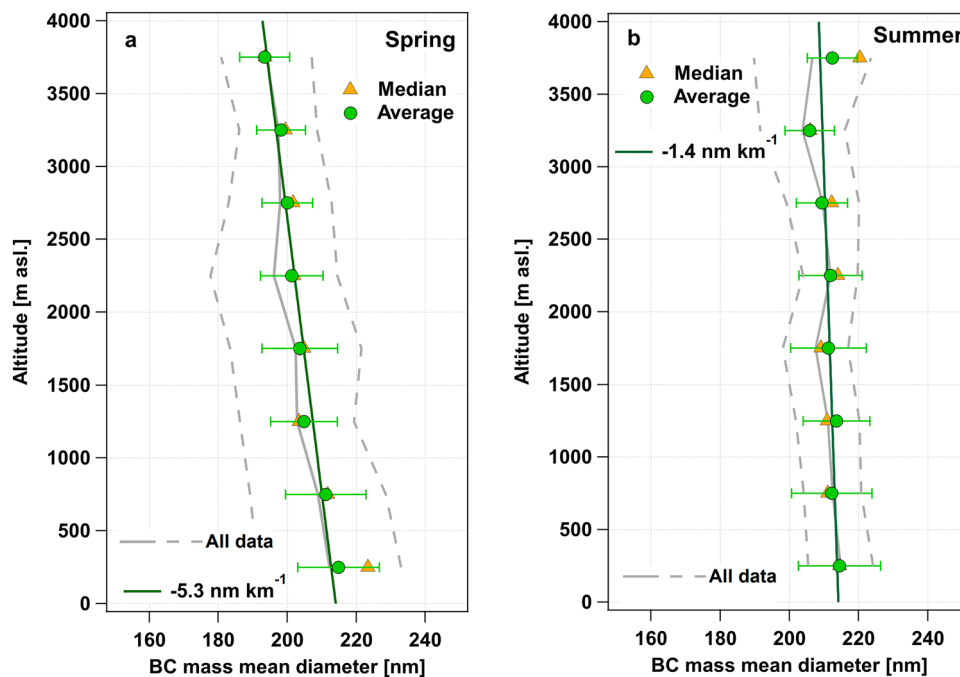


**Fig. 6 The altitude dependence of the BC mass mean diameter.** Round green markers show the average, yellow triangles the median of the BC mass mean diameter in spring (a) and summer (b). The error bars indicate the standard deviation, the green line shows the linear fit to the averages. The gray lines show the average (solid line) and standard deviation (dashed line) of the BC mass mean diameter altitude dependence, if the entire data-set is used including the incomplete profiles as well.

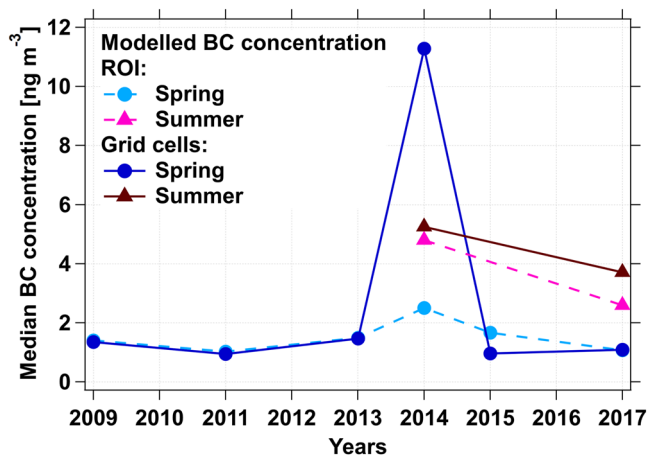


**Fig. 7 Median BC mass concentration, calculated using the OsloCTM3 model's daily averages.** Light markers with dashed lines show data from the complete region of interest (labeled as ROI), and dark markers with solid lines show data from only the grid cells where airborne observations are available (labeled as Grid cells). The pink triangles show model predictions matching the time period of the summer campaigns, whereas the blue round markers indicate spring data.

observations) up to an altitude of  $\sim 2500$  m and extreme high concentrations above that height. This means that  $<2\%$  of the grid cells are affected by this 2014 extreme event, which only has little influence on the calculated average BC properties. The otherwise existing good agreement of the modeled median  $m_{BC}$  provides an indication that our data set might represent well the entire ROI. However, as we will see in the next section, where the average modeled and measured BC concentrations will be compared, strong model-measurement discrepancy exists. Therefore, we have chosen a second approach as well to test the representativeness.

This method uses solely the measurements. The same comparison, as was done with the modeled data, is obviously not possible, but the measured BC properties can be compared to the case, if we only had half of the measurements available. The median  $m_{BC}$  in spring was  $14.3 \text{ ng m}^{-3}$  (Supplementary Table S1, Fig. 2). Each year, half of the grids were randomly selected, the data was deleted, and the median  $m_{BC}$  was calculated using the remaining data. This resulted in a median  $m_{BC}$  of  $13.2 \text{ ng m}^{-3}$  close to the value of  $14.3 \text{ ng m}^{-3}$ . If the same procedure is repeated with the summer data we get  $3.9$  versus  $4.4 \text{ ng m}^{-3}$ . If having only half of the measured data available, do not cause a strong change in the derived average BC properties, then we can assume that having twice as much data or even having data from all of the grids (i.e., from the complete ROI) will also not result in very different values. Therefore, our geographically limited BC observation data set could be considered representative for the entire ROI, the Canadian and European Arctic.

**Comparison between modeled and measured BC concentration.** In this section, the results of a comparison between modeled and measured BC concentrations using the OsloCTM3 model is shown by the ratios between the averaged measured and modeled data. Daily mean (for all days when measurements were carried out during a given campaign/year) modeled BC mass concentrations were used and recalculated to the same three-dimensional grid that was defined treating the measurements. The presented measurement data are the same that were shown in Fig. 4, using only those observations where at least six out of the possible eight altitude grids contain valid observations for a certain year, latitude and longitude values. Two different sets of the modeled data were used: one taking data from the exact same three-dimensional grids where measurements are available (Fig. 8 orange markers), in the second one the modeled BC profiles were calculated and averaged over the whole ROI (Fig. 8 red markers). A perfect agreement between the measurement and model would result in a factor of one.



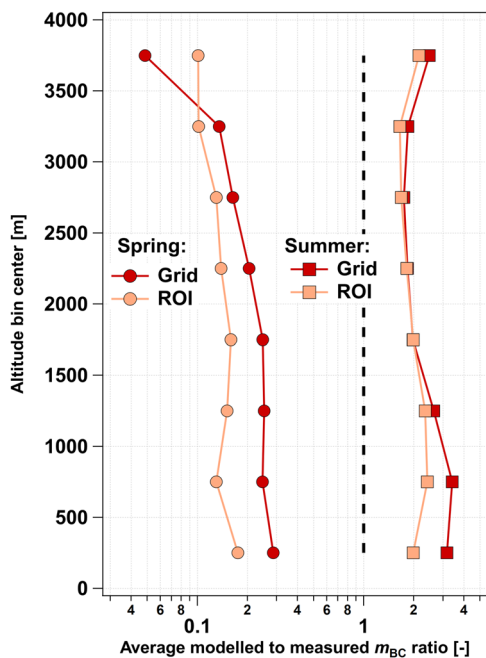


**Fig. 8 Ratios between the modeled and measured  $m_{BC}$  as function of the altitude.** Round markers show spring data, whereas the squares show summer data. The orange markers show the ratios considering modeled BC data from the exact same grid cells as observations are available (labelled as Grid), the red markers were calculated taking the complete ROI (labelled as ROI) into account for the model. The vertical, dashed, black line shows the factor of unity.

Important features can be identified in Fig. 8. Firstly, it is obvious that high and systematic model-measurement discrepancies exist. During spring, the model underestimates observed concentrations, on average the measured  $m_{BC}$  is almost a factor five higher than the modeled one. In summer the simulated concentrations are substantially higher, on average by a factor 3.3, than the observations at all altitudes. If we consider the modeled data from the entire ROI (Fig. 8 red markers), the picture remains the same, strong underprediction by the model in spring and strong overprediction in summer. Contrary to the value of  $m_{BC}$ , one feature is well captured by the model, the average altitude dependency of  $m_{BC}$ , where the average concentration remains nearly constant or decreases only slightly with altitude in both seasons.

As discussed in the introduction, the underestimation of springtime Arctic BC has been identified as a common issue of global atmosphere and climate models for a long time<sup>42–45</sup>. Significant work has gone into understanding the processes that underlie this bias between simulated and observed BC concentrations in the region, resulting in improvements in the model skill. A number of studies have pointed to the importance of aging and removal processes for the long-range transport and deposition of BC in the Arctic<sup>56–62</sup>. Other studies show contributions from factors such as model resolution<sup>63</sup>, convective transport<sup>64</sup>, initial assumptions about the physical properties of the aerosols<sup>65</sup>, representation of supersaturation<sup>66</sup>, and emissions from flaring<sup>67,68</sup> and wildfires<sup>52</sup>. However, many, although not all, of these studies focus on individual parameterizations, processes, or parameters and/or conduct single model studies. Similar degrees of improvement can hence be achieved for very different reasons, and it remains challenging to understand if some processes are generally more important than others. Continued research will, therefore, require a closer integration between models and measurements, and the translation of

observationally-derived process understanding into model parameterizations.

Moreover, measurements in the Arctic continue to be sparse and often cover only smaller regions, single stations, or shorter time periods and individual years. In this manuscript, we have presented an observationally-derived study on BC concentrations and other properties in the Canadian and European Arctic, for two seasons. While the spatial coverage of the observational data is incomplete, comparisons with the output from an updated chemical transport model indicates that the results are broadly representative for the study region. No data set of similar level of detail and spatial, temporal coverage is presently available in the literature. Therefore, our combined data are of high value for model-observation comparisons, and for process studies with global and Arctic focused climate models, as well as for understanding the overall anthropogenic influence on the Arctic regions through emissions of BC.

## Methods

**Aircraft operations.** The BC measurements were carried out aboard the Alfred Wegener Institut's research aircraft Polar 5 and Polar 6 (Basler BT-67) between 2009 and 2017 in the Arctic during several intensive campaigns. Both aircraft are specifically modified for polar research missions including the ability to fly at low cruising speeds ( $185\text{--}400\text{ km h}^{-1}$ ) within an altitude range from 60 to 8000 m. During each flight campaign, meteorological (ambient temperature, pressure and relative humidity) and other auxiliary parameters (aircraft position, altitude, speed) were recorded with 1 Hz time resolution. A more detailed description on Polar 5 and Polar 6 and their different scientific setups can be found elsewhere<sup>69</sup>. We present measurement results from eight individual flight campaigns, six of them were performed in spring, two of them in summer. Table 1 shows a list of aircraft campaigns including duration and aircraft operation base, for the exact flight days and measurement hours we refer to Supplementary Table S2.

**BC measurements.** Aerosol particles were sampled through a total aerosol inlet, a shrouded stainless-steel inlet diffuser with an intake diameter of 0.35 cm, located ahead of the engines. It provides a transmission efficiency close to unity in the particle diameter range of 20 nm–1  $\mu\text{m}$  at the typical cruising airspeeds<sup>70</sup>. The intake was connected inside the cabin to a stainless-steel manifold. The aircraft cabin temperature was always at least 15 °C warmer than the ambient temperature, therefore, no active particle drier was needed to reduce the relative humidity of the aerosol sample below 30%. During one of the campaigns (ACLOUD - Arctic Cloud Observations Using airborne measurements in polar Day conditions) in early summer 2017, the BC instrumentation was operated behind a counterflow virtual impactor inlet<sup>71</sup> and not only out-of-cloud, but also in-cloud measurements were performed. The counterflow virtual impactor inlet has a lowest cut-off diameter of  $\sim 10\ \mu\text{m}$  (dependent on the counterflow), and therefore can sample cloud droplet residuals. When Polar 6 aircraft was clearly out of clouds, the counterflow was switched off, and the counterflow virtual impactor inlet was operated as a total aerosol inlet. In this study only out-of-cloud BC measurements were used, when the inlet sampled all aerosol particles and not the droplet residuals.

The refractory BC<sup>46</sup> properties were measured by a single particle soot photometer (Droplet Measurement Technologies, Longmont, CO, USA) during all aircraft campaigns shown here. The SP2 is able to detect individual BC-containing particles and measure their BC mass in the mass equivalent diameter range of 70–80 nm to 300–800 nm (dependent on the exact instrument type and sensitivity), assuming void-free bulk material density of  $1.8\text{ g cm}^{-3}$ <sup>72</sup>. We used this mass equivalent diameter when referring to the size of the refractory BC particles throughout the manuscript. The SP2's single particle detection is based on laser-induced-incandescence method, absorbing particles are heated up by a continuous-wave, high-intensity, intracavity laser (Nd: YAG crystal, wavelength of 1060 nm) until the refractory part of the particle reaches its vaporization temperature and emits incandescent light. The detected incandescent light's peak intensity is proportional to the BC mass of the particle which is derived after a calibration with standard material with known BC mass<sup>72,73</sup>. The SP2 instruments involved in this study were calibrated before the measurement campaign and most of the time during and after it as well using size selected fullerene soot or Aquadag particles<sup>54,72,74</sup>. Considering that the SP2 has a higher sensitivity to Aquadag particles, we applied a correction to all the calibration curves that were gained using Aquadag based on the work of Laborde et al.<sup>54</sup> to match the fullerene soot sensitivity the best, which produces a calibration curve very similar to ambient BC. In the manuscript we refer to all of our measured refractory BC properties as BC properties for simplicity.

From the individual measurement campaigns BC data within a different diameter range could be collected, because different SP2 instruments can have different mass detection limits. To make the data from the different campaigns comparable, we defined a common BC diameter range of 80–500 nm to use for all flight campaigns. This range covers the diameter range where most of the BC mass

is found (indicated by the shape of the measured mass size distributions). During the first two measurement campaigns, early-version SP2s having a low upper diameter detection limit (230 nm during PAMARCMIP 2011 and 350 nm during PAMARCMIP 2009) were deployed. During the rest of the campaigns the upper detection limit was above 500 nm. We have chosen to extrapolate the measured BC mass size distributions up to 500 nm from the first two campaigns rather than to ignore a big part of the measured mass size distribution (covering 10–30% of the measured BC mass) from the remaining six measurement campaigns. The extrapolation was done by fitting a lognormal function to the BC mass size distribution, and the fit was used in the missing size range (230 or 350–500 nm). The validity of this interpolation method was checked by performing the same fit procedure on data from one of the campaigns where the full BC range (up to 500 nm) could be captured by the SP2.  $m_{BC}$  in the diameter range of 80–500 nm was calculated using the lognormal fit either from 230 nm or from 350 nm on. These values were then compared to the  $m_{BC}$  value which was derived from the complete measured mass size distribution. In any of the considered cases <3% difference in the derived  $m_{BC}$  was found, and therefore we do not introduce considerable error with our BC mass extrapolation.

**Data treatment and aggregation.** On a fast-moving platform such as an airplane great geographical distance can be present between capturing BC-containing particles necessarily contributing to a single BC mass/number size distribution. In this study we present average Arctic BC properties rather than short-term and short-range variations, therefore we have chosen a broad averaging method to treat our measured data. Our data set cover a wide three-dimensional geographical space (65°–90° N latitude, 140° W–20° E longitude and 60–4000 m altitude) and time period (2009–2017), including great part of the European and Canadian Arctic. This geographical space is called our region of interest. The ROI was split into 5° latitude times 5° longitude times 500 m altitude times 1 year four-dimensional units (called grids or grid cells). Within a grid, all aircraft measurements were collected independently of the flight pattern, and with this, all registered BC particles within a grid were considered to calculate the BC properties of interest. After manual inspection of each grid, we have decided to set a limit of at least 400 detected BC-containing particles to consider it for further analysis. Having less particles in a grid resulted in a mass size distribution with too much noise and therefore these were excluded from the study.

Calculating average properties for stationary measurements is straight-forward by time-averaging. This method could not be applied here, the measurement time spent at different locations varied greatly, and therefore some regions would have contributed to the average with a much higher weight than others. The applied gridding of the data overcomes this problem, calculating statistical values of a BC property of all grids guarantees that each grid cell contributes to the average (or other value in question) with the same weight. The different BC parameters presented in this study are introduced in Table 2.

**Oslo CTM3 model.** BC concentrations derived from the SP2 measurements are compared with concentrations simulated for the corresponding years by the OsloCTM3<sup>75,76</sup>. The OsloCTM3 is a global chemical transport model driven by meteorological forecast data from the European Centre for Medium-range Weather Forecast (ECMWF) OpenIFS model. The model is run in a 2.25° × 2.25° horizontal resolution, with 60 vertical levels (the uppermost centered at 0.1 hPa). Anthropogenic emissions are from the Community Emission Data System (CEDS, release version 2017<sup>77</sup>), extended from 2014 to 2017 with emissions from the Shared Socioeconomic Pathways SSP2-4.5<sup>78</sup>. Biomass burning emissions used the Global Fire Emissions Database version 4 (GFED4<sup>79</sup>). In the current model version, BC is treated by a bulk scheme, with being characterized by its total mass. Upon emission, 80% of BC is assumed to be non-hygroscopic and 20% to be hygroscopic. Subsequent transfer from non-hygroscopic to hygroscopic mode is represented by latitudinally and seasonally varying fixed aging rates, derived from simulations with a microphysical aerosol parameterization M7<sup>18</sup>. Aerosols are removed from the atmosphere by dry deposition or washout by convective and large-scale rain. Details about the parameterizations of transport and removal can be found elsewhere<sup>76</sup>.

## Data availability

The location-dependent average BC properties from the individual grids are available in PANGAEA data repository under <https://doi.org/10.1594/PANGAEA.955179>.

## Code availability

The wavemetrics IGOR pro 7 toolkit, SP2 toolkit 4.115 for the analysis of the data from the single particle soot photometer is available under <https://doi.org/10.5281/zenodo.3575186>.

Received: 7 August 2022; Accepted: 8 March 2023;

Published online: 24 March 2023

## References

1. Jeffries, M. O., Overland, J. E. & Perovich, D. K. The Arctic shifts to a new normal. *Phys. Today* **66**, 35–40 (2013).
2. Arctic Climate Change Update 2021: Key Trends and Impacts. Summary for Policymakers. 16pp (Arctic Monitoring and Assessment Programme (AMAP), 2021).
3. Naik, V. et al. *Short-lived climate forcers*, chap. 6 (Cambridge University Press, 2021).
4. Bond, T. C. et al. Bounding the role of black carbon in the climate system: a scientific assessment. *J. Geophys. Res.-Atmos.* **118**, 5380–5552 (2013).
5. Ramanathan, V. & Carmichael, G. Global and regional climate changes due to black carbon. *Nat. Geosci.* **1**, 221–227 (2008).
6. Mitchell, M. Visual range in the polar regions with particular reference to the Alaskan Arctic. *J. Atmos. Terrestrial Phys. Special Suppl.*, 195–211 (1956).
7. Barrie, L. A. Arctic air pollution: an overview of current knowledge. *Atmos. Environ.* **20**, 643–663 (1986). First International Conference on Atmospheric Sciences and Applications to Air Quality.
8. Shaw, G. E. The Arctic haze phenomenon. *B. Am. Meteorol. Soc.* **76**, 2403–2414 (1995).
9. Croft, B. et al. Processes controlling the annual cycle of Arctic aerosol number and size distributions. *Atmos. Chem. Phys.* **16**, 3665–3682 (2016).
10. Willis, M. D., Leitch, W. R. & Abbatt, J. P. Processes controlling the composition and abundance of Arctic aerosol. *Rev. Geophys.* **56**, 621–671 (2018).
11. Sharma, S., Lavoué, D., Cachier, H., Barrie, L. A. & Gong, S. L. Long-term trends of the black carbon concentrations in the Canadian Arctic. *J. Geophys. Res.-Atmos.* **109**, D15 (2004).
12. Sharma, S., Andrews, E., Barrie, L. A., Ogren, J. A. & Lavoué, D. Variations and sources of the equivalent black carbon in the high Arctic revealed by long-term observations at Alert and Barrow: 1989–2003. *J. Geophys. Res.-Atmos.* **111**, D14 (2006).
13. Eleftheriadis, K., Vratolis, S. & Nyeki, S. Aerosol black carbon in the European Arctic: Measurements at Zeppelin station, Ny-ålesund, Svalbard from 1998–2007. *Geophys. Res. Lett.* **36**, 2 (2009).
14. Gogoi, M. M. et al. Aerosol black carbon over Svalbard regions of Arctic. *Polar Sci.* **10**, 60–70 (2016).
15. Schmeisser, L. et al. Seasonality of aerosol optical properties in the Arctic. *Atmos. Chem. Phys.* **18**, 11599–11622 (2018).
16. Stohl, A. Characteristics of atmospheric transport into the Arctic troposphere. *J. Geophys. Res.-Atmos.* **111**, D11 (2006).
17. Shindell, D. T. et al. A multi-model assessment of pollution transport to the Arctic. *Atmos. Chem. Phys.* **8**, 5353–5372 (2008).
18. Lund, M. T. & Berntsen, T. Parameterization of black carbon aging in the OsloCTM2 and implications for regional transport to the Arctic. *Atmos. Chem. Phys.* **12**, 6999–7014 (2012).
19. Ikeda, K. et al. Tagged tracer simulations of black carbon in the Arctic: transport, source contributions, and budget. *Atmos. Chem. Phys.* **17**, 10515–10533 (2017).
20. Xu, J.-W. et al. Source attribution of Arctic black carbon constrained by aircraft and surface measurements. *Atmos. Chem. Phys.* **17**, 11971–11989 (2017).
21. Zhao, N. et al. Responses of Arctic black carbon and surface temperature to multi-region emission reductions: a hemispheric transport of air pollution phase 2 (HTAP2) ensemble modeling study. *Atmos. Chem. Phys.* **21**, 8637–8654 (2021).
22. Tritscher, T. et al. Changes of hygroscopicity and morphology during ageing of diesel soot. *Environ. Res. Lett.* **6**, 034026 (2011).
23. Martin, M. et al. Hygroscopic properties of fresh and aged wood burning particles. *J. Aerosol Sci.* **56**, 15–29 (2013).
24. Flanner, M. G., Zender, C. S., Randerson, J. T. & Rasch, P. J. Present-day climate forcing and response from black carbon in snow. *J. Geophys. Res.-Atmos.* **112**, D11 (2007).
25. Backman, J., Schmeisser, L. & Asmi, E. Asian emissions explain much of the Arctic black carbon events. *Geophys. Res. Lett.* **48**, e2020GL091913 (2021).
26. Review of observation capacities and data availability for Black Carbon in the Arctic region: EU Action on Black Carbon in the Arctic - Technical Report. 35pp (Arctic Monitoring and Assessment Programme (AMAP), 2019).
27. Spackman, J. R. et al. Aircraft observations of enhancement and depletion of black carbon mass in the springtime Arctic. *Atmos. Chem. Phys.* **10**, 9667–9680 (2010).
28. Brock, C. A. et al. Characteristics, sources, and transport of aerosols measured in spring 2008 during the aerosol, radiation, and cloud processes affecting Arctic climate (ARCPAC) project. *Atmos. Chem. Phys.* **11**, 2423–2453 (2011).
29. Wofsy, S. C. HIAPER pole-to-pole observations (HIPPO): fine-grained, global-scale measurements of climatologically important atmospheric gases and aerosols. *Philos. T. R. Soc. A* **369**, 2073–2086 (2011).
30. Konovalov, I. B. et al. Estimation of black carbon emissions from Siberian fires using satellite observations of absorption and extinction optical depths. *Atmos. Chem. Phys.* **18**, 14889–14924 (2018).
31. Brock, C. A. et al. Ambient aerosol properties in the remote atmosphere from global-scale in situ measurements. *Atmos. Chem. Phys.* **21**, 15023–15063 (2021).

32. Herber, A. B. et al. Regular airborne surveys of Arctic sea ice and atmosphere. *Eos Transact. AGU* **93**, 41–42 (2012).
33. Schulz, H. et al. High Arctic aircraft measurements characterising black carbon vertical variability in spring and summer. *Atmos. Chem. Phys.* **19**, 2361–2384 (2019).
34. Wendisch, M. et al. The Arctic cloud puzzle: Using ACloud/PASCAL multiplatform observations to unravel the role of clouds and aerosol particles in Arctic amplification. *B. Am. Meteorol. Soc.* **100**, 841–871 (2019).
35. Wendisch, M. et al. Atmospheric and surface processes, and feedback mechanisms determining arctic amplification: a review of first results and prospects of the (AC)3 project. *B. Am. Meteorol. Soc.* <https://doi.org/10.1175/BAMS-D-21-0218.1> (2023).
36. Ferrero, L. et al. Vertical profiles of aerosol and black carbon in the arctic: a seasonal phenomenology along 2 years (2011–2012) of field campaigns. *Atmos. Chem. Phys.* **16**, 12601–12629 (2016).
37. Markowicz, K. et al. Vertical variability of aerosol single-scattering albedo and equivalent black carbon concentration based on in-situ and remote sensing techniques during the iarea campaigns in ny-Ålesund. *Atmos. Environ.* **164**, 431–447 (2017).
38. Cappelletti, D. et al. Vertical profiles of black carbon and nanoparticles pollutants measured by a tethered balloon in longyearbyen (svalbard islands). *Atmos. Environ.* **290**, 119373 (2022).
39. Bates, T. S. et al. Measurements of atmospheric aerosol vertical distributions above Svalbard, Norway, using unmanned aerial systems (UAS). *Atmos. Meas. Tech.* **6**, 2115–2120 (2013).
40. Samset, B. H. et al. Black carbon vertical profiles strongly affect its radiative forcing uncertainty. *Atmos. Chem. Phys.* **13**, 2423–2434 (2013).
41. Sand, M. et al. Aerosols at the poles: an AeroCom phase ii multi-model evaluation. *Atmos. Chem. Phys.* **17**, 12197–12218 (2017).
42. Eckhardt, S. et al. Current model capabilities for simulating black carbon and sulfate concentrations in the Arctic atmosphere: a multi-model evaluation using a comprehensive measurement data set. *Atmos. Chem. Phys.* **15**, 9413–9433 (2015).
43. Chen, X., Kang, S. & Yang, J. Investigation of distribution, transportation, and impact factors of atmospheric black carbon in the Arctic region based on a regional climate-chemistry model. *Environ. Pollut.* **257**, 113127 (2020).
44. Srivastava, R. & Ravichandran, M. Spatial and seasonal variations of black carbon over the Arctic in a regional climate model. *Polar Sci.* **30**, 100670 (2021). Special Issue on “Polar Studies - Window to the changing Earth”.
45. Whaley, C. H. et al. Model evaluation of short-lived climate forcers for the Arctic monitoring and assessment programme: a multi-species, multi-model study. *Atmos. Chem. Phys.* **22**, 5775–5828 (2022).
46. Petzold, A. et al. Recommendations for reporting “black carbon” measurements. *Atmos. Chem. Phys.* **13**, 8365–8379 (2013).
47. Schwarz, J. P. et al. Global-scale seasonally resolved black carbon vertical profiles over the Pacific. *Geophys. Res. Lett.* **40**, 5542–5547 (2013).
48. Zanatta, M. et al. Effects of mixing state on optical and radiative properties of black carbon in the European Arctic. *Atmos. Chem. Phys.* **18**, 14037–14057 (2018).
49. Sharma, S. et al. An evaluation of three methods for measuring black carbon in Alert, Canada. *Atmos. Chem. Phys.* **17**, 15225–15243 (2017).
50. Ohata, S. et al. Estimates of mass absorption cross sections of black carbon for filter-based absorption photometers in the Arctic. *Atmos. Meas. Tech.* **14**, 6723–6748 (2021).
51. Taketani, F. et al. Shipborne observations of atmospheric black carbon aerosol particles over the Arctic Ocean, Bering Sea, and North Pacific Ocean during September 2014. *J. Geophys. Res.-Atmos.* **121**, 1914–1921 (2016).
52. Ohata, S. et al. Arctic black carbon during pamarcmip 2018 and previous aircraft experiments in spring. *Atmos. Chem. Phys.* **21**, 15861–15881 (2021).
53. Matsui, H., Hamilton, D. S. & Mahowald, N. M. Black carbon radiative effects highly sensitive to emitted particle size when resolving mixing-state diversity. *Nat. Comm.* **9**, 3446 (2018).
54. Laborde, M. et al. Sensitivity of the single particle soot photometer to different black carbon types. *Atmos. Meas. Tech.* **5**, 1031–1043 (2012).
55. Moteki, N. et al. Size dependence of wet removal of black carbon aerosols during transport from the boundary layer to the free troposphere. *Geophys. Res. Lett.* **39**, 13 (2012).
56. Bourgeois, Q. & Bey, I. Pollution transport efficiency toward the Arctic: Sensitivity to aerosol scavenging and source regions. *J. Geophys. Res.-Atmos.* **116**, D8 (2011).
57. Browse, J., Carslaw, K. S., Arnold, S. R., Pringle, K. & Boucher, O. The scavenging processes controlling the seasonal cycle in Arctic sulphate and black carbon aerosol. *Atmos. Chem. Phys.* **12**, 6775–6798 (2012).
58. Fan, S.-M. et al. Inferring ice formation processes from global-scale black carbon profiles observed in the remote atmosphere and model simulations. *J. Geophys. Res.-Atmos.* **117**, D23 (2012).
59. Kipling, Z. et al. What controls the vertical distribution of aerosol? relationships between process sensitivity in HadGEM3–UKCA and inter-model variation from AeroCom phase ii. *Atmos. Chem. Phys.* **16**, 2221–2241 (2016).
60. Mahmood, R. et al. Seasonality of global and Arctic black carbon processes in the Arctic monitoring and assessment programme models. *J. Geophys. Res.-Atmos.* **121**, 7100–7116 (2016).
61. Lund, M. T., Berntsen, T. K. & Samset, B. H. Sensitivity of black carbon concentrations and climate impact to aging and scavenging in OsloCTM2–M7. *Atmos. Chem. Phys.* **17**, 6003–6022 (2017).
62. Liu, M. & Matsui, H. Improved simulations of global black carbon distributions by modifying wet scavenging processes in convective and mixed-phase clouds. *J. Geophys. Res.-Atmos.* **126**, e2020JD033890 (2021).
63. Sato, Y. et al. Unrealistically pristine air in the arctic produced by current global scale models. *Sci. Rep.* **6**, 26561 (2016).
64. Allen, R. J. & Landuyt, W. The vertical distribution of black carbon in cmip5 models: comparison to observations and the importance of convective transport. *J. Geophys. Res.-Atmos.* **119**, 4808–4835 (2014).
65. Han, Y. et al. Impact of the initial hydrophilic ratio on black carbon aerosols in the arctic. *Sci. Tot. Environ.* **817**, 153044 (2022).
66. Matsui, H. & Liu, M. Importance of supersaturation in arctic black carbon simulations. *J. Climate* **34**, 7843 – 7856 (2021).
67. Stohl, A. et al. Black carbon in the Arctic: the underestimated role of gas flaring and residential combustion emissions. *Atmos. Chem. Phys.* **13**, 8833–8855 (2013).
68. Cho, M.-H. et al. A missing component of arctic warming: black carbon from gas flaring. *Environ. Res. Lett.* **14**, 094011 (2019).
69. Alfred-Wegener-Institut Helmholtz-Zentrum für Polar- und Meeresforschung. Polar aircraft Polar5 and Polar6 operated by the Alfred Wegener Institute. *J. Large-Scale Res. Facil.* **2**, A87 (2016).
70. Leaitch, W. R. et al. Effects of 20–100 nm particles on liquid clouds in the clean summertime Arctic. *Atmos. Chem. Phys.* **16**, 11107–11124 (2016).
71. Ehrlich, A. et al. A comprehensive in situ and remote sensing data set from the Arctic cloud observations using airborne measurements during polar day (ACLOUD) campaign. *Earth Syst. Sci. Data* **11**, 1853–1881 (2019).
72. Moteki, N. & Kondo, Y. Dependence of laser-induced incandescence on physical properties of black carbon aerosols: Measurements and theoretical interpretation. *Aerosol Sci. Tech.* **44**, 663–675 (2010).
73. Schwarz, J. P. et al. Single-particle measurements of midlatitude black carbon and light-scattering aerosols from the boundary layer to the lower stratosphere. *J. Geophys. Res.-Atmos.* **111**, D16 (2006).
74. Gysel, M., Laborde, M., Olfert, J. S., Subramanian, R. & Gröhn, A. J. Effective density of Aquadag and fullerene soot black carbon reference materials used for SP2 calibration. *Atmos. Meas. Tech.* **4**, 2851–2858 (2011).
75. Søvdø, O. A. et al. The chemical transport model Oslo CTM3. *Geosci. Model Dev.* **5**, 1441–1469 (2012).
76. Lund, M. T. et al. Short black carbon lifetime inferred from a global set of aircraft observations. *npj Climate Atmos. Sci.* **1**, 1 (2018).
77. Hoesly, R. M. et al. Historical (1750–2014) anthropogenic emissions of reactive gases and aerosols from the community emissions data system (CEDS). *Geosci. Model Dev.* **11**, 369–408 (2018).
78. Fricko, O. et al. The marker quantification of the shared socioeconomic pathway 2: A middle-of-the-road scenario for the 21<sup>st</sup> century. *Global Environ. Change* **42**, 251–267 (2017).
79. van der Werf, G. R. et al. Global fire emissions estimates during 1997–2016. *Earth Syst. Sci. Data* **9**, 697–720 (2017).
80. Lampert, A. et al. The spring-time boundary layer in the central Arctic observed during PAMARCMiP 2009. *Atmosphere* **3**, 320–351 (2012).

## Acknowledgements

We gratefully acknowledge the funding by the Deutsche Forschungsgemeinschaft (DFG, German Research Foundation) – Projektnummer 268020496 – TRR 172, within the Transregional Collaborative Research Center “Arctic Amplification: Climate Relevant Atmospheric and Surface Processes, and Feedback Mechanisms (AC)3”. Next to it the authors would like to thank all participants of the aircraft campaigns who made the collection of this BC data set possible. Authors would like to thank Canadian Forces Services at Alert, NU for helping with station logistics for POLAR5 and 6, scientific directions and participation of Drs. Richard Leaitch and Shao-Meng Li during some campaigns and technicians for installation and calibrations of scientific instruments. M.T.L. and B.H.S. acknowledge funding from the Research Council of Norway through the QUISARC project (grant number 248834). R.B.S. acknowledges funding from the Research Council of Norway (grant number 314997). M.Z. acknowledges funding by the Deutsche Forschungsgemeinschaft (DFG, German Research Foundation, grant no. Projektnummer 457895178). The authors acknowledge support by the Open Access Publication Funds of Alfred-Wegener-Institut Helmholtz-Zentrum für Polar- und Meeresforschung.

## Author contributions

Z.J. analyzed, interpreted the data and wrote the paper. M.Z. was responsible for the BC measurements during several aircraft campaigns and helped in the data interpretation. M.T.L. analyzed the model data and prepared it for the comparison, wrote parts of the

paper. B.H.S. helped with the model interpretation and discussion. R.B.S. run the model and prepared its output. S.S. took part in several campaigns and conducted BC measurements. M.W. coordinated many of the aircraft campaigns, and substantively revised the paper. A.H. organized and supervised all aircraft campaigns and supervised this work. All authors read, commented and discussed the paper.

### Funding

Open Access funding enabled and organized by Projekt DEAL.

### Competing interests

The authors declare no competing interests.

### Additional information

**Supplementary information** The online version contains supplementary material available at <https://doi.org/10.1038/s43247-023-00749-x>.

**Correspondence** and requests for materials should be addressed to Zsófia Jurányi.

**Peer review information** *Communications Earth & Environment* thanks the anonymous reviewers for their contribution to the peer review of this work. Primary Handling

Editors: Kerstin Schepanski and Clare Davis. Peer reviewer reports are available.

**Reprints and permission information** is available at <http://www.nature.com/reprints>

**Publisher's note** Springer Nature remains neutral with regard to jurisdictional claims in published maps and institutional affiliations.



**Open Access** This article is licensed under a Creative Commons Attribution 4.0 International License, which permits use, sharing, adaptation, distribution and reproduction in any medium or format, as long as you give appropriate credit to the original author(s) and the source, provide a link to the Creative Commons license, and indicate if changes were made. The images or other third party material in this article are included in the article's Creative Commons license, unless indicated otherwise in a credit line to the material. If material is not included in the article's Creative Commons license and your intended use is not permitted by statutory regulation or exceeds the permitted use, you will need to obtain permission directly from the copyright holder. To view a copy of this license, visit <http://creativecommons.org/licenses/by/4.0/>.

© The Author(s) 2023